QUARTERLY JOURNAL OF THE ROYAL METEOROLOGICAL SOCIETY
Q. J. R. Meteorol. Soc. **134**: 301–315 (2008)
Published online 28 March 2008 in Wiley InterScience
(www.interscience.wiley.com) DOI: 10.1002/qj.202

Scaling turbulent atmospheric stratification. II: Spatial stratification and intermittency from lidar data

M. Lilley,[a,d] S. Lovejoy,[a,e]* K. B. Strawbridge,[b] D. Schertzer[c,f] and A. Radkevich[a,g]

[a] *Department of Physics, McGill University, Montreal, Canada*
[b] *Centre for Atmospheric Research Experiments, Science and Technology Branch, Environment Canada, Egbert, Canada*
[c] *CEREVE, Ecole Nationale des Ponts et Chaussées, Marne-la-Vallée, France*
[d] *GreCo, Institut d'Astrophysique de Paris, 98bis Boulevard Arago, 75014 Paris, France*
[e] *Centre GEOTOP UQAM/McGill, Université du Québec, Montréal, Canada*
[f] *Météo France, 1 Quai Branly, Paris 75007, France*
[g] *Candian Centre for Remote Sensing, 588 Booth Street, Ottawa, Ontario, Canada*

ABSTRACT: We critically re-examine existing empirical studies of vertical and horizontal statistics of the horizontal wind and find that the balance of evidence is in favour of the Kolmogorov $k_x^{-5/3}$ scaling in the horizontal, Bolgiano-Obukov scaling $k_z^{-11/5}$ in the vertical corresponding to a $D_s = 23/9$ stratified atmosphere in (x, y, z) space. This interpretation is particularly compelling once one recognizes that the 23/9-D turbulence can lead to long-range biases in aircraft trajectories and hence to spurious statistical exponents in wind, temperature and other statistics reported in the literature. Indeed, we show quantitatively that one is easily able to reinterpret the major aircraft-based campaigns (GASP, MOZAIC) in terms of the model. In part I, we have seen that this model is compatible with 'turbulence waves' which can be close to classical linear gravity waves in spite of their very different nonlinear mechanism. We then use state-of-the-art lidar data of atmospheric aerosols (considered as passive tracers) in order to obtain direct estimates of the effective ('elliptical') dimension of the spatial part: $D_s = 23/9 = 2.55 \pm 0.02$. This result essentially rules out the standard 3-D or 2-D isotropic theories or the anisotropic quasi-linear gravity wave theories which have $D_s = 3$, 2, 7/3 respectively.

In this paper we focus on the multifractal (intermittency) statistics showing that there is a very small but apparently real variation in the value of D_s, ranging for the weak and intense structures so that D_s ranges from roughly 2.53 to 2.57. We also show that the passive scalars are well approximated by universal multifractals; we estimate the exponents to be $\alpha_h = 1.82 \pm 0.05$, $\alpha_v = 1.83 \pm 0.04$, $C_{1h} = 0.037 \pm 0.0061$ and $C_{1v} = 0.059 \pm 0.007$ (h for horizontal, v for vertical).

KEY WORDS fractal; multifractal; atmospheric spectrum; lidar; passive scalar

Received 9 December 2005; Revised 10 October 2007; Accepted 23 November 2007

1. Introduction

In part I (Lovejoy *et al*., 2008c), we argued that the 23/9-D model with the extension to partially unlocalized propagators for the observable (e.g. velocity, density) fields provided the most physically satisfactory model of the stratified atmosphere, being based on two turbulent fluxes, (the energy and buoyancy force variance fluxes), respecting generalized Kolmogorov and Corrsin–Obukov laws and having some wave phenomenology. In this paper, we examine the corresponding spatial empirical evidence. In particular, we directly determine H_z (the ratio of horizontal to vertical scaling exponents) using nine airborne lidar vertical cross-sections of atmospheric aerosol covering the range 3 m to 4500 m in the vertical (a factor of 1500), and 100 m to 120 km in the horizontal (a factor of 1200). One important difference between such airborne lidar measurements and *in situ* aircraft measurements is that the former do not suffer from aircraft trajectory biases. This is because airborne lidar is a remote-sensing technique in which ground is used as the reference 'altitude'. The key result of this experiment – announced in Lilley *et al*. (2004) – is convincing evidence for the 23/9-D model. It yields $H_z = 0.55 \pm 0.02$ and therefore $D_s = 2.55 \pm 0.02$ so that the 2-D and 3-D theories are well outside the one standard deviation error bars. These error bars are particularly small since each of the nine 2-D sections have several orders of magnitude more data than the largest comparable balloon experiments (Table I). Here, the aerosols act as a tracer, and laser light is scattered back to a telescope in the aircraft enabling a 2-D reconstruction of its spatial distribution. This in turns allows the determination of the degree of stratification of structures as functions of their horizontal extents. The horizontal range is particularly significant since it spans the critical 10 km scale where the 3-D to 2-D transition – the mesoscale gap – has been postulated to occur. In addition, each dataset is obtained within a short

* Correspondence to: S. Lovejoy, Department of Physics, McGill University, 3600 University St, Montreal, Quebec, Canada, H3A 2T8.
E-mail: lovejoy@physics.mcgill.ca

Table I. A review of some of the existing empirical evidence for the scaling of atmospheric horizontal wind, temperature and density in the vertical direction (β_v). Note that these spectra were typically obtained for a very limited range of scales, often over less than an order of magnitude. Our estimates of β_v (footnotes) are from the graphs in the published papers and are therefore somewhat subjective.

Author and year	Experimental Technique	Quantity measured	Observations made by author	Ratio of largest to smallest scales	Altitude range	Spectral exponent measured
Endlich *et al.* (1969)	Balloon sonde	Horizontal wind velocity fluctuations	Compatible with $\beta_v = 11/5$	100	0–16 km	$\beta_v = 2.2$–2.5
Adelfang (1971)[a]	1183 Jimsphere profiles	Horizontal wind velocity fluctuations	No theoretical explanation offered	100	3–21 km	$\beta_v \sim 2.1$–2.5 (inferred from structure function)
Van Zandt (1982)[b]	1200 Jimspheres	Horizontal wind velocity fluctuations	Claims $\beta_v = 2.4$ 'universal' spectrum close to ocean result of Garrett and Munk (1972)	10	4–16 km	$\beta_v \sim 2.2$–2.5
Schertzer and Lovejoy (1985)[c]	80 balloon sonde profiles	Horizontal velocity	Compatible with 23/9-D unified scaling, $\beta_v = 11/5$	64	Troposphere	$\beta_v \sim 2.2$ (determined as $1 + 2H_v$, $H_v = 0.60$)
Fritts and Chou (1987)[d]	MST radar	Horizontal wind velocity fluctuations	Compatible with saturated gravity wave model and separability	<10	Lower stratosphere	$\beta_v = 3$
Fritts *et al.* (1988)[e]	Radar and balloon sounding	Horizontal wind velocity fluctuations	Compatible with saturated gravity wave model	10	Lower stratosphere, troposphere	$\beta_v = 3$
Tsuda *et al.* (1989)[f]	MST radar	Horizontal wind velocity fluctuations	Compatible with saturated gravity wave model	10	Stratosphere, mesosphere, troposphere	Nonlinear regression is made by the author $\beta_v \approx 2.2$
Beatty *et al.* (1992)[g]	Raleigh/Na lidar	Density fluctuations	–	10	Stratopause, mesopause	Stratopause: $\beta_v = 2.2$–2.4 Mesopause: $\beta_v = 2.9$–3.2
Lazarev *et al.* (1994)	287 balloon sondes	Horizontal velocity, 50 m resolution in vertical	Compatible with 23/9-D unified scaling, $\beta_v = 11/5$	250	Troposphere	β_v of the mean $= 2.2$; individual exponents 1.5–3.5, median $= 2$.
Allen and Vincent (1995)[h]	18 locations in Australia, each with 300–1300 soundings	Temperature	–	30	Stratosphere, troposphere	Stratosphere: $\beta_v \sim 2.2$–2.6, Troposphere: $\beta_v \sim 2.7$–3.1
Gardner *et al.* (1995)	Na wind temperature lidar, 1km vertical resolution	Temperature	Supports DFT	–	Mesophere	$\beta_v = 2.5 \pm 0.1$

DOI: 10.1002/qj

Table I. (*Continued*).

Author and year	Experimental Technique	Quantity measured	Observations made by author	Ratio of largest to smallest scales	Altitude range	Spectral exponent measured
Gao (1998)[i]	Na lidar	Temperature and density fluctuations	Concludes that the vertical wind data is incompatible with linear saturation theory (Smith *et al.*, 1987) and diffusive filtering theory (Gardner, 1994)	10	84 to 100 km	Temperature: $\beta_v \sim 2.5$ Density: $\beta_v \sim 3.5$
Cot (2001)[j]	70 high-resolution balloon sondes	Horizontal wind shear and temperature	Slope claimed (2.5–3) compatible with saturated gravity waves	30	100 m to 25 km	Reference lines with $\beta_v = 2.8–3$ for horizontal wind (about the same for temperature)

[a] Two locations, different times of year and altitudes. Radar-tracked Jimspheres are among the most accurate sondes with resolutions in the vertical of around 50 m.
[b] The vertical spectra were reproduced from an unpublished NASA report by GE Daniels. Proposed a variant of the Garrett–Munk oceanic gravity wave model.
[c] Probability distributions were used to estimate H_v (part I, section 2).
[d] See comments in the text.
[e] An exponent $\beta_v = 11/5$ gives a good fit for troposphere, stratosphere and mesosphere. 1-hour averaging, low-pass filtering, 3 km smoothing applied.
[f] An exponent $\beta_v = 11/5$ is compatible with the spectrum. 1-hour averages, 3 km smoothing applied.
[g] Low-pass filter applied. Effort made to isolate individual gravity wave events. (Quasi-monochromatic waves should not be confused with continuous spectra. Over the range 100 m to 1 km, depending on location, we find that exponents 2.2–2.4 are reasonable.
[h] Individual sonde data were normalized before averaging; this reduces low-frequency energies.
[i] Low-pass filtering applied.
[j] This was a 'very high resolution' (100 m) custom-built balloon sonde. Over the range 100 m to 1 km, the value $\beta_v = 11/5$ fits very well, especially to the horizontal velocity spectra.

DOI: 10.1002/qj

period of time (about 20 minutes) so that the meteorology is roughly constant. The result is almost exactly that predicted from the 23/9-D model and shows that, even at scales as small as 3 m, the atmosphere does not appear to be three-dimensional, nor at large scales does it ever appear to be perfectly flat (i.e. 2-D). Rather, structures simply become more and more (relatively) flat as they get larger.

2. Brief review of the empirical evidence

2.1. Scaling in the vertical direction

Although there is still no consensus about the nature of the empirical horizontal spectrum (the 2-D versus 3-D debate or the various gravity wave theories), in the vertical, things are a little easier if only because it is easier for a single experiment to cover much of the dynamical range. The 23/9-D theory was motivated by the conclusions of the empirical campaign in Landes (Schertzer and Lovejoy, 1985) and by the radiosonde observations of horizontal wind shear along the vertical made by Endlich *et al*. (1969) and Jimsphere observations by Adelfang (1971). At about the same time, VanZandt (1982) proposed an anisotropic $k_h^{-\beta}$ (horizontal), $k_v^{-\beta}$ (vertical), gravity wave theory with $\beta_h = 5/3$, $\beta_v = 2.4$; recent variants (with $\beta_v = 3$ instead; it is significant that the original $\beta_v = 2.4$ is very close to the value 11/5 of the 23/9-D model and close to dropsonde estimates; Lovejoy *et al*., 2007) were discussed in part I. Table I summarizes and compares some of the vertical studies, focusing on the horizontal wind and temperature. The most important general conclusion is the consensus about the fact that there is scaling in the vertical with $\beta_v > \beta_h$, i.e. there is no evidence of isotropic turbulence at any scale (a point made forcefully on the basis of 5 m resolution dropsonde data in Lovejoy *et al*. (2007)). Recall that $\beta_v > \beta_h$ implies that the atmosphere is differentially stratified, becoming increasingly flat at larger and larger scales. Although the interpretations of the campaigns were made from the perspective of various gravity wave theories, the actual spectral exponents (β_v; Table I, especially the footnotes) are in fact generally much closer to the Bolgiano–Obhukov (BO) value of 11/5 than the standard gravity wave value of 3.

It is somewhat surprising that, contrary to the situation in convectively driven laboratory flows, in the recent atmospheric literature the theoretical prediction of Bolgiano (1959) and Obukhov (1959) is rarely discussed, possibly because of the belief that it is not compatible with wave phenomenology. Discussions related to the isotropic BO scaling on the effect of buoyancy, stratification and convection on the spectrum and the Bolgiano length l_B (at which the transition from 3-D isotropic $k^{-5/3}$ turbulence to anisotropic 3-D $k^{-11/5}$ turbulence supposedly takes place) can be found mostly in literature on the buoyancy-driven Rayleigh–Benard laboratory experiments (discussion in Lilley *et al*., 2004).

It is interesting to note that there is evidence from work in progress on numerical weather models (by some of the authors with J. Stolle) that $H_v \approx 0.75$ (and hence $\beta_v \approx 1 + 2\ H_v \approx 2.5$), so that these results may be close to those of at least some numerical models. In addition, according to the results of Lovejoy *et al*. (2007) on 2772 H_v estimates for 1 km thick vertical layers, that H_v for the horizontal wind slowly increases from $\approx 3/5$ near the surface to 0.75 at altitudes of several kilometres (with intermittency corrections this leads to $\beta \approx 2.4$). The Kolmogorov value $H_v = 1/3$ was found only $\approx 0.1\%$ of the time while the 2-D turbulence/gravity wave value $H_v = 1$ was found only $\approx 0.3\%$ of the time. At present, the relationship between this result and those reported here for passive scalar surrogates is not clear.

2.2. Scaling in the horizontal direction

The early claims about the horizontal spectra (in particular the influential Van der Hoven (1957) spectra) were taken in the time domain and converted into horizontal spatial spectra by using Taylor's (1938) hypothesis of 'frozen turbulence'. This assumption was originally made as a basis for analyzing laboratory turbulence flows in which a strong scale separation exists between the forcing and the turbulence; one simply converts from time to space using a constant (e.g. mean large-scale) velocity assuming that the turbulent fluctuations are essentially 'frozen' with respect to the rapid advection of structures transported by the mean flow. In the atmosphere, the validity of this assumption depends on the existence of a clear large-scale/small-scale separation. The difficulties in interpretation are illustrated by the debate prompted by the early studies – especially Van der Hoven (1957) – which were strongly criticized by Goldman (1968), Pinus (1968) and Vinnichenko (1969) and indirectly by Hwang (1970). For instance, after commenting that if the mesoscale gap (separating the small-scale 3-D regime from the large-scale 2-D regime) really existed, it would be only for less than 5% of the time, Vinnichenko (1969) even noted that Van der Hoven's spectrum was actually the superposition of four spectra – including a high-frequency one taken under 'near-hurricane' conditions.

In order to obtain direct estimates of horizontal wind spectra, Brown and Robinson (1979) used the standard meteorological measuring network, but the scales were very large and intermittency was so strong that they could not obtain unambiguous results. A more direct way to obtain true horizontal spectra is to use aircraft data, and indeed, since the 1980s, there have been two ambitious experiments (Global Atmospheric Sampling Program, GASP, and Measurement of Ozone and water vapour by Airbus In-service Aircraft, MOZAIC) to collect large amounts of horizontal wind data, using commercial airliners fitted with anemometers. The basic problem here is that aircraft are affected by turbulent updraughts and tail winds so that their trajectories can have long-range correlations with the turbulent structures they are

DOI: 10.1002/qj

trying to measure. In other words, the interpretation of *in situ* measurements themselves requires a theory of turbulence. For example, if one accepts that the large scale is flat (2-D), then the vertical variability is small so that we expect that deviations of the aircraft from a perfect straight-line horizontal trajectory will be small and that the effect of the turbulent motion on the aircraft will be negligible. Similarly, if one is in an isotropic 3-D regime, then there is only one exponent (the same in every direction) so that if one finds scaling, it is natural to interpret this in terms of the unique scaling exponent of the regime.

In a recent paper (Lovejoy *et al*., 2004), it was shown that due to the effects of anisotropic (presumably 23/9-D) turbulence, aircraft can fly over distances of hundreds of kilometres in the stratosphere on trajectories whose fractal dimension is close to 14/9 rather than 1, i.e. they are strongly biased by the turbulence that they measure. In this case, the long-range bias was the result of using a 'Mach cruise' autopilot that enforced correlations between the temperature and the aircraft speed, such that the Mach number was constant to within ±2%. Even when the trajectory has $D = 1$ in a 23/9-D turbulence, the aircraft does not fly at a perfectly flat trajectory but rather at an average slope s, then the scale function (see part I) of the vertical vector $(\Delta x, \Delta z)$ is

$$\| (\Delta x, \Delta z) \| = \| (\Delta x, s\Delta x) \| \approx \Delta x + l_s \left(\frac{s\Delta x}{l_s} \right)^{1/H_z},$$

where l_s is the sphero-scale, and $H_z = 5/9$. From this we see that there is a critical distance $\Delta x_c = l_s s^{1/(H_z - 1)}$ such that the second (vertical) term dominates the scale function so that for larger distances, the statistics will be those of the vertical rather than the horizontal. Figures 1(a) and (b) show that the wind statistics from GASP and MOZAIC – which are the two largest-scale experimental campaigns to date – can readily be explained in the context of the 23/9-D model with only very small average aircraft slopes. We find that if we take $l_s = 4$ cm (the stratospheric value found by the NASA ER-2 aircraft, but also similar to the values found below for lidar backscatter), then the low-frequency regimes of both of the experiments can be fairly well explained in this way.

At first sight, if interpreted as a slope with respect to the horizontal, $s = 1.5$ m km^{-1} is perhaps more than might have been expected (although as an average for 'flat' legs of a commercial jet, it is probably not so large). However, it is a slope with respect to the eigenvector of the **G** matrix discussed in part I; if there are even small off-diagonal elements (corresponding to non-orthogonal eigenvectors), even a trajectory perfectly 'flat' in the sense of being rigorously perpendicular to the local gravity vector may still have slope of 1.5 m km^{-1} with respect to the eigenvector. Since the scale function emerges as a consequence of two highly variable fluxes, it may be expected that the **G** matrix (and hence eigenvectors) are somewhat variable from place to place (nonlinear generalized scale invariance, GSI).

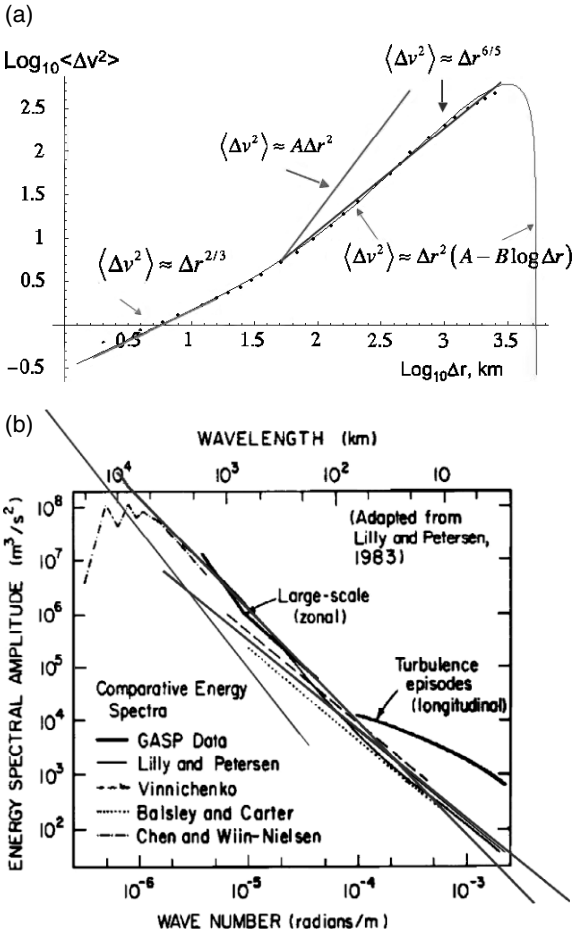

Figure 1. (a) Replotted from a graph of the second-order velocity structure function from Lindborg and Cho (2001). Straight reference lines show (from left to right) the Kolmogorov, BO and 2-D turbulence behaviours. The $\langle \Delta v^2 \rangle \approx \Delta r^{6/5}$ reference line corresponds to a slope of 1.5 m km^{-1} and a sphero-scale of 4 cm. The curved line in the right half is the log-corrected quadratic from Lindborg and Cho (2001). The extension of this line (not shown in Lindborg and Cho) rapidly leads to impossible negative structure functions (b) Adapted from Gage and Nastrom (1986). The reference lines which extend outside the box have been added; from left to right, they have slopes −3, −5/3, and −11/5. (2-D turbulence/gravity waves, Kolmogorov and Bolgiano-Obukhov values respectively). This figure is available in colour online at www.interscience.wiley.com/qj

This allows the possibility for off-diagonal elements in **G** and hence for non-orthogonal eigenvectors. Finally, the estimate $s = 1.5$ m km^{-1} is based on a ball-park estimate of the sphero-scale; if the sphero-scale is smaller than 4 cm, the required slope will also be smaller.

From Figure 1(a), we see that the aircraft inertial scale is roughly $\Delta x_i = 20$ km (the end of the Kolmogorov 2/3 power regime), while at roughly $\Delta x_f = 75$ km, the slope follows more closely a BO 6/5 power law (the extra factors of 2 in the exponents come from using the variance). The (possibly fractal) transition zone is roughly between 20 and 75 km. It is interesting to compare this to the theoretical 2-D turbulence reference line (a pure quadratic law), as well as the log-corrected quadratic law (curved line) using the coefficients from Cho and Lindborg (2001), Lindborg and Cho (2001). We see that,

DOI: 10.1002/qj

while it is possible to use log corrections to make a quadratic mimic a 6/5 power law over a limited range, as soon as we go a little outside the fitted range (not shown in Lindborg and Cho, 2001), the curve rapidly leads to impossible negative structure functions.

Turning to the GASP experiment, we show Figure 1(b) adapted from Gage and Nastrom (1986). Concentrating on the more reliable solid black lines, which result from the data-intensive GASP experiment (and ignoring the selected 'turbulent episode' subset) we see that the BO blue line does an excellent fit from 20 km upwards. Once again, if the tropospheric sphero-scale $= 4$ cm, then we find that an average aircraft slope of roughly 1.5 m km^{-1} explains the GASP spectra. Note that, unlike the case of stratospheric trajectories where a significant fractal regime was observed (from roughly 3 to 300 km), in this case the regime is either short or does not affect the scaling of the horizontal significantly; a small slope is sufficient.

Not only does it seem that the 23/9-D theory is the only one that can account for these major horizontal spectral studies, but results of satellite studies of cloud radiances provide additional support. Although cloud radiances are not directly related to the horizontal wind, the two fields are nonetheless strongly nonlinearly coupled such that if the scale-invariant symmetry is broken in one, it will almost certainly be broken in the other. This was the motivation of the area perimeter (Lovejoy, 1982) and a series of other studies (Lovejoy *et al*., 1993; Lovejoy *et al*., 2001; Lovejoy and Schertzer, 2006) culminating in the recent reflectivity factor, visible, infrared and passive microwave results from the Tropical Rainfall Measuring Mission (TRMM; Lovejoy *et al*., 2008a, 2008b; Figure 2 in part I). The latter study used about 1000 times the amount of data of the previous ones (about 1000 orbits), and showed that, to within typically about $\pm 1\%$, the radiance gradients followed multiplicative cascade statistics from 5000 km down to the resolution of the measurements, i.e. <10 km). It is not obvious how several different horizontal regimes could be hiding in this data. At the same time, multifractal cloud simulations (including those based on the turbulence/wave model, part I) show how strong scaling horizontal anisotropy permitted by GSI (with off-diagonal elements in the horizontal part of **G**), can reconcile the wide diversity of cloud morphology, texture and type with the isotropic statistics which essentially wash out most of the anisotropy.

2.3. Lidar and direct measurements of differential stratification

During the 1980s and 1990s, there was growing evidence in favour of the 23/9-D model. This evidence was mostly indirect since vertical and horizontal statistics have almost invariably been studied in separate experiments in separate regions of the world and at different times. Until the lidar study (Lilley *et al*., 2004), the only exceptions were the radar rain study (Lovejoy *et al*., 1987) which only had a factor of 8 in scale in the vertical, and the roughly simultaneous aircraft radiosonde studies reported in Chiginiskaya *et al*. (1994) and Lazarev *et al*. (1994). Direct tests of the fundamental prediction of differential stratification of structures have been lacking since they could only be obtained remotely by near-instantaneous vertical cross-sections. Thanks to developments in high-powered lidar – primarily the ability to digitize each pulse in real time with a wide dynamic range using logarithmic amplifiers – this type of data is now available. The lidar measures the backscatter ratio (B, the ratio of aerosol backscatter to background molecular scattering) of aerosols far from individual point sources; the measured backscatter ratio is taken as a surrogate for the concentration of a passively advected tracer.

Here we use lidar data which were taken as part of the PACIFIC 2001 airborne lidar experiment using an airborne lidar platform called AERIAL (AERosol Imaging Airborne Lidar) flown at a constant altitude over a grid of flight legs of roughly 100 km in the Lower Fraser Valley (British Columbia, Canada). Although the airborne lidar platform is a simultaneous up–down system mounted aboard the NRC-CNRC Convair 580 aircraft, only data from the downward-pointing system was used. The lasers operated at the fundamental wavelength of 1.064 m (suited for the detection of particles of the order of 1 m), with a pulse repetition rate of 20 Hz. The output power of the downward lidar was measured to be 450 mJ. The beam divergence was 6.6 mrad. The detectors employed were 35.6 cm Schmidt–Cassegrain telescopes with an 8 mrad field-of-view which focused the captured photons onto 3 mm avalanche photodiodes (APD). Each telescope was interfaced with the APD using custom-designed coupling optics. The downward lidar APD and optics were connected to a logarithmic amplifier designed to increase the dynamic range. The data acquisition system consisted of two 100 Mhz 12-bit A/D cards with a Pentium 550 Hz computer that controlled the laser interlock system, and collected, stored and displayed the data in real time. The use of a logarithmic amplifier was very important since without it – given the $1/(\text{range})^2$ fall-off of the power with range – the dynamic range of the signal would have been too limited; it would have displayed spuriously smooth fields.

The datasets consisted of B measurements made continuously in a 2-D planar region. One dimension was along the propagation axis (the vertical), and the other was along the displacement of the aircraft, i.e. along horizontal straight paths at a fixed altitude of 4500 m. The horizontal extents of the datasets were up to 120 km, while the spatial resolution in the horizontal was set by the aircraft speed and laser shot averaging to 100 m. The vertical extents were of the order of 4500 m and the spatial resolution was equal to the pulse length of 3 m. Therefore, the ratio of the largest to the smallest scales achieved was in the range 500–1000 and 1000–1500 in the horizontal and vertical, respectively. Figure 2(a) shows a typical vertical–horizontal cross-section and Figure 2(b) is a 'zoom' showing the incredible detail now available. Also noticeable is the fact that, while the large scales are horizontally stratified, the small scales are

DOI: 10.1002/qj

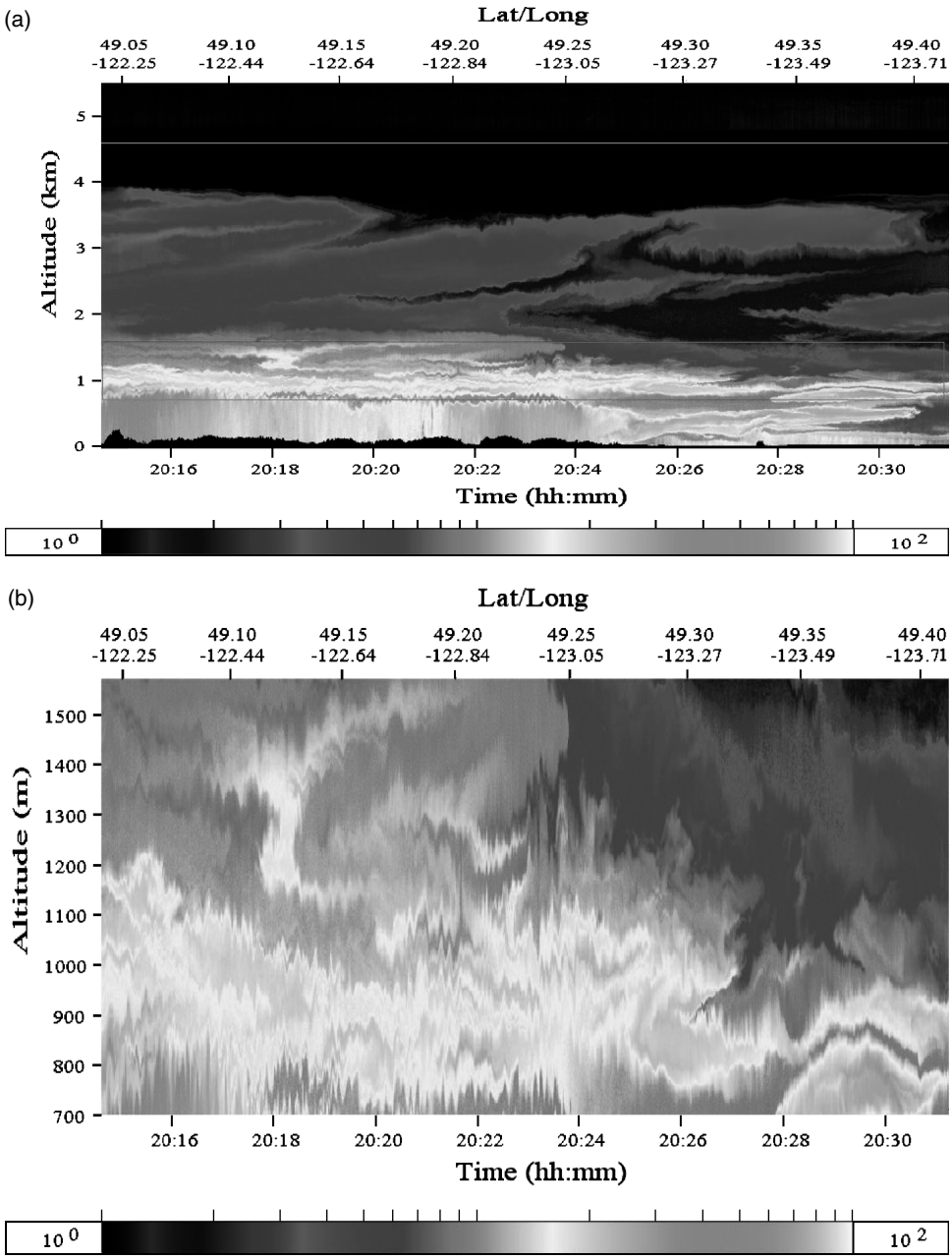

Figure 2. (a) Typical vertical-horizontal cross section acquired on August 14 2001. The scale (bottom) is logarithmic: darker is for smaller backscatter (aerosol density surrogate), lighter is for larger backscatter. The black shapes along the bottom are mountains in the British Columbia region. The line at 4.6 km altitude shows the aircraft trajectory (b) Enlarged content of the (700–1600 m) box in (a). Note that small structures become more vertically aligned while large structures are fairly flat. The aspect ratio is 0.016. This figure is available in colour online at www.interscience.wiley.com/qj

much less so showing more and more vertically aligned structures at the smaller scales – exactly as predicted by the 23/9-D model.

These data were analyzed by Lilley (2003) and a brief 'announcement' paper (Lilley *et al.*, 2004) gave the key anisotropy results for first-order structure functions and (second-order) spectra. Below, our goal is to consider all the moments (i.e. including the intermittency), however we quickly review the Lilley *et al.* (2004) results.

Analyzing the first-order moment ($q = 1$) case is interesting (Figure 3), because we expect $K(1)$ to be small enough that the horizontal H_h and vertical H_v can be estimated as $\xi_h(1) \approx H_h = 1/3$, $\xi_v(1) \approx H_v = 3/5$. (Throughout this paper, $K(q)$ is the scaling exponent function for the passive scalar flux $\varphi = \chi^{3/2}\varepsilon^{-1/6}$ (see section 3.1), whereas in part I, the $K(q)$ refers to energy flux ε.) We can see from the figure that not only is the scaling excellent in both horizontal and vertical directions, but in addition that the exponents are very close to those expected theoretically. In fact, we find from linear regression that $H_h = 0.33 \pm 0.03$, $H_v = 0.60 \pm 0.04$. Also visible in the figure is the scale at which the functions cross; this is a direct estimate of the sphero-scale which we find here varies between 2 cm and 80 cm, with an average of 10 cm.

DOI: 10.1002/qj

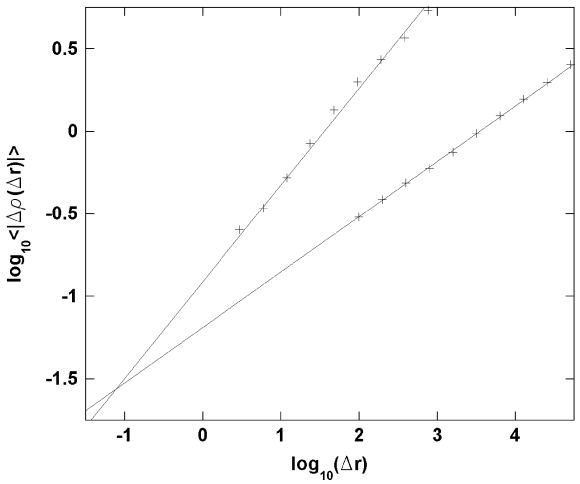

Figure 3. The symbols show the first-order vertical structure function, and first-order horizontal structure function for the ensemble of nine vertical airborne lidar cross-sections. ρ is the dimensionless backscatter ratio, the surrogate for the passive scalar aerosol density. Δr is either the vertical or horizontal distance (m). The lines have the theoretical slopes 3/5, 1/3; they intersect at the sphero-scale here graphically estimated as $\approx$10 cm.

A standard method for the analysis of scaling and turbulent fields is the calculation of energy spectra. Lilley *et al*. (2004) find excellent scaling despite the slight increase at high wavenumber which is due to the presence of instrument noise. We have already noted that for isotropic scaling systems $E(k) = k^{-\beta}$; since $E(k)$ is the Fourier transform of the autocorrelation, we have a simple relation between β and $\xi(2)$:

$$\beta = 1 + \xi(2) = 1 + 2H - K(2) \tag{1}$$

From the analysis below, we find $K_{\mathrm{h}}(2) = 0.065$, $K_{\mathrm{v}}(2) = 0.10$, hence the theoretical spectral exponents are: $\beta_{\mathrm{h}} = 1.60$, $\beta_{\mathrm{v}} = 2.10$; these are within one standard deviation of the regression values $\beta_{\mathrm{h}} = 1.61 \pm 0.03$, $\beta_{\mathrm{v}} = 2.15 \pm 0.04$ reported in Lilley *et al*. (2004).

In Figure 3 it is important to realize that only the intercepts of these first-order structure functions were fitted to the data; the slopes have the theoretical values indicated. These first simultaneous measurements on atmospheric cross-sections permitted Lilley *et al*. (2004) to estimate the elliptical dimension D_s as $2 + H_{\mathrm{h}}/H_{\mathrm{v}} = 2.55 \pm 0.02$, clearly eliminating the contending 2-D theory or leading gravity wave theory (which have $D_s = 2$ and 7/3, respectively).

The first- and second-order statistics are only very partial descriptions of the fields. In order to more completely test the anisotropic 23/9-D multifractal model discussed in part I, we must investigate the statistics of all orders, i.e. including the intermittency. (In part III we also indicate how to verify the theory for arbitrary directions using a new Anisotropic Scaling Analysis Technique (ASAT)). In particular, we are interested in testing the hypothesis that (a) the passive scalar field is a universal multifractal, and (b) the lower- and higher-order statistics (which correspond to weak or strong structures/events) are stratified in the same way as the mean (and variance) fields investigated in Figure 3.

3. Direct test of the 23/9-D model using atmospheric aerosols and lidar data

3.1. The statistics of passive scalar advection

3.1.1. The anisotropic Corrsin–Obukov law

In optically thin media, the backscatter ratio B (or possibly B raised to a power B^{η}; Lilley *et al*., 2004) is a good surrogate for the aerosol concentration. If one assumes that the sources and sinks of aerosols are far enough removed from the region that the latter may be assumed statistically homogeneous, and if one assumes that one can neglect chemical reactions occurring during the roughly 20 minutes during which the data were acquired, then B will be an approximation to a passively advected tracer ('scalar'; with or without wave-like fractional integration). We now consider the predictions of the 23/9-D model for such passive scalars. By introducing the scale function, the 23/9-D model automatically predicts anisotropic generalizations of many of the standard results of isotropic turbulence theory, including the standard Obukhov (1949) and Corrsin (1951) theory of passive scalar advection. The standard isotropic theory is based on two quadratic invariants: the energy flux for the wind field (section 2.2.3) and the passive scalar variance flux χ, so that for statistically isotropic passive scalar concentrations ρ:

$$\Delta\rho(\Delta\mathbf{r}) = \chi^{1/2}_{|\Delta\mathbf{r}|}\varepsilon^{-1/6}_{|\Delta\mathbf{r}|}|\Delta\mathbf{r}|^{1/3};$$
$$\Delta\rho(\Delta\mathbf{r}) = \rho(\mathbf{r} + \Delta\mathbf{r}) - \rho(\mathbf{r}). \tag{2}$$

The subscripts indicate the spatial resolutions of the fluxes. As discussed in part I, in order to obtain the anisotropic generalization of Equation (2), we need only to make the replacement $|\Delta\mathbf{r}| \rightarrow \| \Delta\mathbf{r}\|$ (the spatial scale function; see part I for a definition and part III for space–time). Taking $\|(\Delta x, 0, 0)\| = \Delta x$, $\|(0, 0, \Delta z)\| = l_s(\Delta z/l_s)^{1/H_z}$ and $l_s = \varepsilon^{5/4}/\phi^{3/4}$, where ϕ is the buoyancy variance flux and l_s is the sphero-scale (see part I, in particular, appendix A for technical details including the distinction between the bare and dressed sphero-scale), this yields the following horizontal and vertical laws:

$$\Delta\rho(\Delta x) = \varphi^{1/3}_{\Delta x}\Delta x^{1/3}; \quad \varphi_{\Delta x} = \chi^{3/2}_{\Delta x}\varepsilon^{-1/2}_{\Delta x}$$
$$\Delta\rho(\Delta z) = \kappa^{1/5}_{\Delta z}\Delta z^{3/5}; \quad \kappa_{\Delta z} = \chi^{5/2}_{\Delta z}\varepsilon^{-5/2}_{\Delta z}\phi_{\Delta z}. \tag{3}$$

The first is the standard Corrsin–Obukhov law while the second is new. Although any power of φ or κ could also have been used, the particular choice in Equation (3) was made for convenience since with the transformation $\varphi \rightarrow \varepsilon$; $\kappa \rightarrow \phi$, the resulting anisotropic passive scalar formalism maps onto the anisotropic Kolmogorov law (for the velocity); we make a few more comments below.

DOI: 10.1002/qj

Although the lidar only measures a surrogate for ρ, according the the 23/9-D model, any physical atmospheric field whose dynamics are controlled by the fluxes ε and ϕ should have the same scale function and hence the same ratio of horizontal to vertical exponents. Hence, the experiment can still estimate H_z and hence D_s even if the relation between B and ρ is nonlinear or is only statistical in nature.

3.1.2. *The statistical moments*

Until now, we have ignored intermittency, concentrating instead on the predictions of spatially homogeneous turbulence theories. However, during the 1980s it became increasingly recognized that turbulent scaling regimes often had cascade phenomenologies generically leading to strong multifractal intermittency. For example, taking qth powers of Equation (2) and performing ensemble averaging, we expect the following statistics in passive scalar advection:

$$\left\langle |\Delta\rho(\Delta\mathbf{r})|^q \right\rangle = \left\langle \varphi^q_{\|\Delta\mathbf{r}\|} \right\rangle \|\Delta\mathbf{r}\|^{q/3}. \tag{4}$$

In part I we show that if we consider data from a single realization over a region width l_x, thickness l_z, we can use the multiplicative property of the cascades to factor the fluxes into low-frequency and high-frequency components allowing us to make the following estimates:

$$\begin{aligned}
&\left(|\Delta\rho(\Delta x, 0, 0)|^q\right)_{(l_x,l_z)} \\
&\approx \varphi_\lambda^{q/3} \left(\frac{l_x}{\Delta x}\right)^{K_\varphi(q/3)} \Delta x^{q/3} = \varphi_\lambda^{q/3} l_x^{K_\varphi(q/3)} \Delta x^{\xi_\varphi(q)}, \\
&\left(|\Delta\rho(0, 0, \Delta z)|^q\right)_{(l_x,l_z)} \\
&\approx \kappa_\lambda^{q/5} \left(\frac{l_z}{\Delta z}\right)^{K_\kappa(q/5)} \Delta z^{3q/5} = \kappa_\lambda^{q/5} l_z^{K_\kappa(q/5)} \Delta z^{\xi_\kappa(q)},
\end{aligned} \tag{5}$$

where the fluxes have the following dependence on the ratio λ over which the cascade is developed:

$$\langle \varphi_\lambda^q \rangle = \lambda^{K_\varphi(q)}; \quad \langle \kappa_\lambda^q \rangle = \lambda^{K_\kappa(q)} \tag{6}$$

and the horizontal (Δx) and vertical (Δz) structure function exponents (subscripts h, v) are:

$$\begin{aligned}
\xi_\mathrm{h}(q) &= q/3 - K_\varphi(q/3), \\
\xi_\mathrm{v}(q) &= 3q/5 - K_\kappa(q/5).
\end{aligned} \tag{7}$$

(For simplicity we suppose horizontal isotropy and do not give explicitly Δy dependencies). We mentioned above that the choice of variables φ, κ was somewhat arbitrary since any of their powers could have been used. Now, we note that although φ, κ are combinations of conserved fluxes, *a priori*, they are not themselves exactly conserved scale by scale (i.e. we do not expect $K_\varphi(1) = 0$, $K_\kappa(1) = 0$ although we expect deviations will be small). Finally, it is tempting to hypothesize the statistical independence of the basic conserved fluxes ε, χ, ϕ; this would imply

$$\begin{aligned}
K_\varphi\left(\frac{q}{3}\right) &= K_\chi\left(\frac{q}{2}\right) + K_\varepsilon\left(\frac{-q}{6}\right) \quad \text{and} \\
K_\kappa\left(\frac{q}{5}\right) &= K_\chi\left(\frac{q}{2}\right) + K_\varepsilon\left(\frac{-q}{2}\right) + K_\phi\left(\frac{q}{5}\right).
\end{aligned}$$

We do not do this because, on the one hand, this is implausible – the real physics undoubtedly involve coupled cascades – and, on the other hand, for positive q it would involve K_ε of negative arguments ($K_\varepsilon(-q/2)$, $K_\varepsilon(-q/6)$) and, for universal multifractals (except when $\alpha = 2$), these are divergent. In the context of a passive scalar treatment of the temperature field, Schmitt *et al.* (1996) have a detailed discussion of this issue and propose a simple alternative. For the moment, due to these theoretical uncertainties, we will adopt a more empirical view and define horizontal and vertical exponents as:

$$\begin{aligned}
\xi_\mathrm{h}(q) &= \xi_\varphi(q) = qH_\mathrm{h} - K_\mathrm{h}(q); \\
H_\mathrm{h} &= 1/3; \quad K_\mathrm{h}(q) = K_\varphi(q/3); \\
\xi_\mathrm{v}(q) &= \xi_\kappa(q) = qH_\mathrm{v} - K_\mathrm{v}(q); \\
H_\mathrm{v} &= 3/5; \quad K_\mathrm{v}(q) = K_\kappa(q/5).
\end{aligned} \tag{8}$$

We can now use the structure function ratio $\xi_\mathrm{h}/\xi_\mathrm{v}$ to determine the anisotropy exponent H_z:

$$\begin{aligned}
H_z &= \xi_\mathrm{h}(q)/\xi_\mathrm{v}(q) = H_{z,1} + \Delta H_z; \\
H_{z,1} &= \frac{H_\mathrm{h}}{H_\mathrm{v}} = \frac{5}{9},
\end{aligned} \tag{9}$$

where ΔH_z is a small intermittency correction and we have introduced $H_{z,1} = 5/9$ with the subscript '1' because if $K_\mathrm{h}(1) = K_\mathrm{v}(1) = 0$, then $H_z = H_{z,1}$. In terms of the Ks, we have:

$$\begin{aligned}
\Delta H_z &= \frac{1}{qH_\mathrm{v}} \frac{\left\{H_{z,1}K_\mathrm{v}(q) - K_\mathrm{h}(q)\right\}}{\{1 - K_\mathrm{v}(q)/(qH_\mathrm{v})\}} \\
&\approx \frac{\left\{H_{z,1}K_\mathrm{v}(q) - K_\mathrm{h}(q)\right\}}{qH_\mathrm{v}}.
\end{aligned} \tag{10}$$

This shows that, unless $K_\mathrm{h}(q)/K_\mathrm{v}(q) = H_{z,1} = 5/9$, there will be intermittency (K-dependent) corrections to the $H_{z,1} = 5/9$ value. Since in multifractals there is a one-to-one correspondence between singularities (structures) and statistical moments, a small q-dependence in H_z implies a small difference in the degrees of stratification of strong and weak structures. This is discussed in more detail in part I appendix A, where we used dropsonde data to estimate ΔH_z for the horizontal wind field. Conversely, the complete absence of such intermittency corrections implies specific statistical dependencies between the fluxes such that, for all q, $K_\mathrm{h}(q)/K_\mathrm{v}(q) = 5/9$.

DOI: 10.1002/qj

In the general cascade theory, the only restriction of $K(q)$ is that it is convex. However, due to the existence of stable, attractive multifractal universality classes (the multiplicative analogue of the additive central limit theorem in probability theory; Schertzer and Lovejoy, 1987, 1997), under fairly general circumstances, $K(q)$ is determined by two basic parameters as:

$$K(q) = \frac{C_1}{\alpha - 1}(q^\alpha - q), \tag{11}$$

where C_1 is the co-dimension characterizing the sparseness of the mean field whereas $0 \leq \alpha \leq 2$ is the index of multifractality (the Levy index of the generator); it characterizes the relative importance of low 'holes' in the field ($\alpha = 0$ is totally hole-dominated; it is the monofractal limiting case). If K_h and K_v are both of the universal form Equation (11), then the condition $K_\mathrm{h}(q)/K_\mathrm{v}(q) = 5/9$ implies that $\alpha_\mathrm{h} = \alpha_\mathrm{v}$ and $C_{1\mathrm{h}}/C_{1\mathrm{v}} = 5/9$.

3.2. Multifractal analysis

3.2.1. qth-order structure functions

Until now, we have only tested the theory in orthogonal directions (coordinate axes) and for first- and second-order moments. In part III we estimate the angle function Θ characterizing the 'trivial anisotropy' using the 'ASAT' technique (see Equation (16), part I). Here, we turn to testing over a wider range of statistical moments, q. We need to compare horizontal and vertical $\xi(q)$ and $K(q)$ exponents. The simplest way is to calculate the structure functions which are simply the moments of the absolute differences (Equation (2)); this is a 'poor man's wavelet', adequate for our purposes. Figures 4(a) and (b) show the scaling in the horizontal and vertical for the structure functions of order $0 \leq q \leq 5$ and Figure 5 shows the corresponding exponents $\xi_\mathrm{h}(q)$, $\xi_\mathrm{v}(q)$ obtained from the slopes. The straight lines qH_h, qH_v are also shown; the deviations are purely due to the multifractal intermittency corrections $K(q)$ which we study in the next subsection.

3.2.2. Trace moments, and C_1

In order to characterize $\xi(q)$, we need to estimate the nonlinear part, $K(q)$. However, due to the fact that the C_1 values are much smaller than the H values, we find that for low q, $K(q)$ will be much smaller than $\xi(q)$. It is therefore best to estimate $K(q)$ directly; this can be done by removing the linear scaling $\|\Delta\mathbf{r}\|^{qH}$ in Equation (4) so as to study the scaling of the fluxes $\left\langle \varphi^q_{\|\Delta\mathbf{r}\|} \right\rangle$ directly. This can be achieved by fractionally differentiating ρ by H_h in the horizontal, and by H_v in the vertical (Figure 6; this is simply a Fourier filter of $k^{H\mathrm{v}}$). In practice, if the H values are <1, it is sufficient to take the modulus of the gradient vector which is a surrogate for the (absolute) first-order derivative, itself a surrogate for the flux at the finest available resolution. From this high-resolution flux estimate, we estimate the flux at lower resolutions by simply spatially degrading it. This 'trace moment' method (Schertzer and Lovejoy, 1987) is fairly standard and has been tested extensively numerically (e.g. Lavallée *et al.*, 1993).

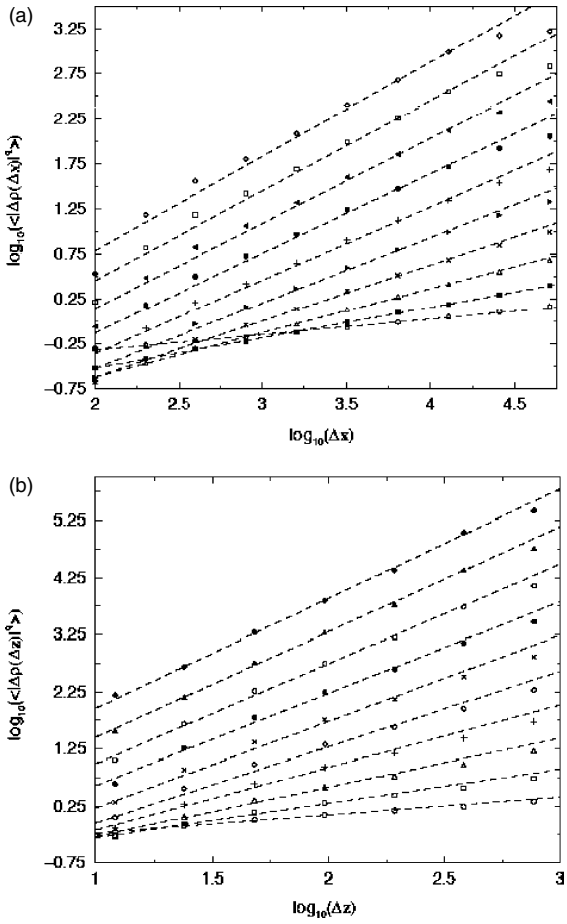

Figure 4. (a) Horizontal and (b) vertical structure functions of order q between 0.5 and 5 at increments of 0.5. The regressions were estimated over the scaling range.

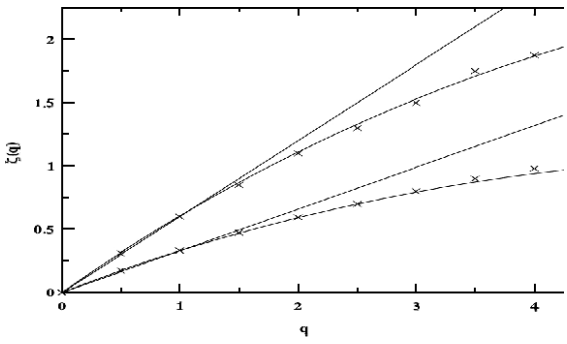

Figure 5. The scaling exponent $\xi(q)$ of the qth-order structure functions; the lower points and curves are for the horizontal direction, the upper points and curves are for the vertical direction. They are determined from the slopes of Figures 4(a) and (b). The straight lines are the basic (non-intermittent) scalings, with slopes 1/3 and 3/5 respectively. The curves are from universal multifractal forms with parameters $C_{1\mathrm{h}} = 0.037$, $\alpha_\mathrm{h} = 1.82$ and $C_{1\mathrm{v}} = 0.059$, $\alpha_\mathrm{h} = 1.83$, respectively.

We have mentioned that the basic characterization of $K(q)$ (obtained as the exponent of $\varphi_{\|\Delta\mathbf{r}\|}$ with scale $\|\Delta\mathbf{r}\|$) is the sparseness of the mean, C_1, and the multifractal index, α (Figures 6(a) and (b)). Using

DOI: 10.1002/qj

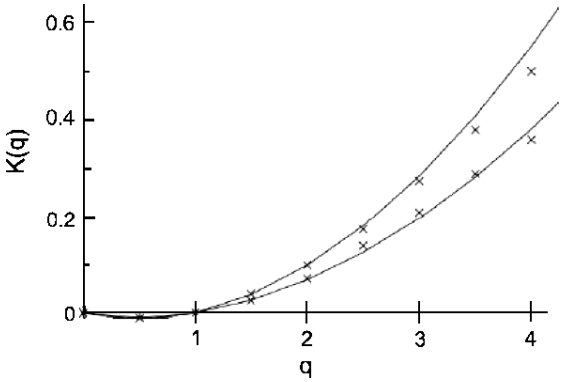

Figure 6. The scaling exponent function $K(q)$ for the horizontal direction (lower points and curve) and vertical direction (upper points and curve), from the slopes of the trace moments in Figures 5(a) and (b), respectively. The curves are regressions to the universal multifractal forms with parameters $C_{1,\mathrm{h}} = 0.037$, $\alpha_{\mathrm{h}} = 1.82$ and $C_{1,\mathrm{v}} = 0.059$, $\alpha_{\mathrm{v}} = 1.83$, respectively.

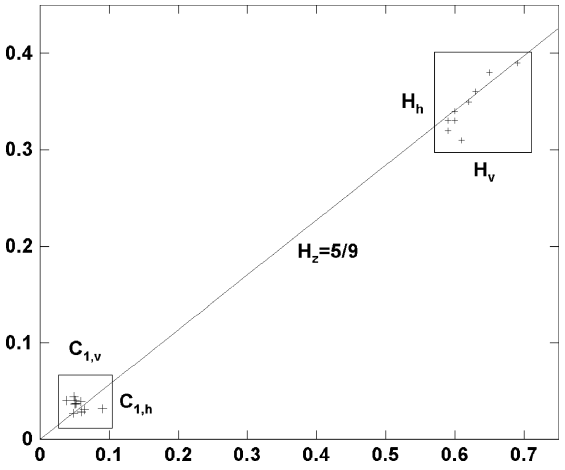

Figure 7. A scatterplot of the basic universal multifractal exponents C_1 and H, as estimated from trace moments and structure functions respectively for each of the nine cross-sections. Shown for reference is the theoretical slope $H_z = 5/9$. The scatter is within a standard error; see the text. This shows that the strong (intermittent) structures are also stratified with roughly the same exponent H_z. The abscissa is a vertical exponent and the ordinate is a horizontal exponent.

moments near unity allows us to use the relation $C_1 = K'(1)$, to estimate C_1 by numerically differentiating $K(q)$. We obtain $C_{1,\mathrm{h}} = 0.037 \pm 0.006$, $C_{1,\mathrm{v}} = 0.059 \pm 0.007$. From Equation (8) we see that, if the universality hypothesis holds and $\Delta H_z = 0$ (see next subsection), the ratio $C_{1,\mathrm{h}}/C_{1,\mathrm{v}} = H_z$ and $\alpha_{\mathrm{h}} = \alpha_{\mathrm{v}}$. In Figure 7 we show the corresponding scatterplot with the H and C_1 values. Due to their much smaller values, the relative spread in the C_1 values is larger than for H. However, when the standard error estimates are included, $C_{1,\mathrm{h}}/C_{1,\mathrm{v}} = 0.70 \pm 0.2$ is within one standard deviation of the theoretical value 5/9.

3.2.3. *Double trace moments and α*

In principle, we could perform a nonlinear regression in $K(q)$ to determine α as well as C_1. In practice however, the regression is not very well posed; this is particularly true since the universal form (Equation (11)) is only valid for q's below a critical value after which $K(q)$ becomes linear. This 'multifractal phase transition' (Schertzer *et al.*, 1993) arises because either the sample size is too small to estimate the high-order moments, or because of the divergence of moments greater than a critical value q_{D} (cf. the value $q_{\mathrm{D}} = 2$ in the turbulence wave model, appendix C of part I, or the empirical value $q_{\mathrm{D}} = 5$ for the velocity (Schertzer and Lovejoy, 1985)). A better way to estimate the value of α is via the 'double trace moment' (DTM) technique. The DTM is essentially the same as the Trace Moment method except that, after fractionally differentiating ρ, at the finest resolution Λ one first takes the η power. One then degrades the resolution to an intermediate resolution λ:

$$\left\langle \left(\varphi_{\Lambda}^{\eta}\right)_{\lambda}^{q} \right\rangle = \lambda^{K(q,\eta)} \tag{12}$$

The new exponent $K(q, \eta)$ is related to $K(q)$ via

$$K(q, \eta) = K(q\eta) - qK(\eta), \tag{13}$$

so that if $K(q) = K(q, 1)$ is of the universal form (11), then we have the particularly simple relation:

$$K(q, \eta) = \eta^{\alpha} K(q, 1) = \eta^{\alpha} K(q), \tag{14}$$

so that for fixed q, α can be determined directly by log–log regression of $K(q, \eta)$ versus η. Figures 8(a) and (b) show the results for $K(q, \eta)$ in the horizontal and vertical respectively. The linearity shows that the universality hypothesis is accurately obeyed. From the regressions, we obtain: $\alpha_{\mathrm{h}} = 1.82 \pm 0.05$, $\alpha_{\mathrm{v}} = 1.83 \pm 0.04$. Consistent with the possibility $\Delta H_z = 0$ (same stratification for intense and weak structures), these are equal within error bars. Finally, from the measured values of α and the regression intercepts $K(q, 1)$, we obtain the additional estimates $C_{1,\mathrm{h}} = 0.037 \pm 0.006$, $C_{1,\mathrm{v}} = 0.059 \pm 0.007$, which are very close to those obtained from the Trace Moment method discussed above.

3.2.4. *The cross-section to cross-section variability*

Until now, we have mostly pooled the data from the nine cross-sections in order to obtain improved statistics. However, it is of interest to confirm that the statistics for individual cross-sections are indeed close to each other, i.e. that they are not from totally different statistical ensembles. Also, since the sphero-scale depends on two highly variable fluxes, we anticipate that it will vary considerably about the ensemble estimate (10 cm). In Table II we give the values of l_{s} and $\langle|\Delta\rho(l_s)|\rangle$; we notice a slight tendency for the larger l_{s} cases (less stratification) to occur when $\langle|\Delta\rho(l_s)|\rangle$ is larger. Overall l_{s} varies from 2 cm to 80 cm. Also, in Table II we see the cross-section to cross-section variation of the universal multifractal parameters; it is generally small.

Overall we find that H_{h} varies between 0.31 and 0.39 with an ensemble mean of 0.33 ± 0.03 while H_{v} varies between 0.59 and 0.69 with an ensemble mean of 0.60 ± 0.04. (Note that the values quoted in the row 'ensemble'

DOI: 10.1002/qj

Table II. A comparison of various universal multifractal parameters, as estimated for each of the nine cross-sections.

Dataset	H_h	H_v	H_z	α_h	α_v	$C_{1,h}$	$C_{1,v}$	$C_{1,h}/C_{1,v}$	$\Delta\rho(l_s)$	l_s (m)
08–14-t5	0.35	0.62	0.56	1.86	1.85	0.031	0.064	0.48	0.018	0.03
08–14-t7	0.36	0.63	0.57	1.82	1.78	0.027	0.048	0.56	0.025	0.03
08–14-t17	0.33	0.59	0.56	1.90	1.90	0.029	0.059	0.49	0.050	0.79
08–14-t20	0.34	0.60	0.56	1.90	1.85	0.044	0.049	0.89	0.056	0.63
08–15-t20	0.31	0.61	0.51	1.80	1.80	0.040	0.039	1.02	0.022	0.10
08–15-t2	0.33	0.60	0.55	1.77	1.81	0.037	0.052	0.71	0.020	0.08
08–15-t6	0.39	0.69	0.56	1.87	1.80	0.039	0.059	0.66	0.063	0.31
08–15-t8	0.38	0.65	0.58	1.76	1.80	0.040	0.050	0.80	0.036	0.10
08–15-t22	0.32	0.59	0.54	1.85	1.85	0.037	0.051	0.72	0.045	0.31
Ensemble	**0.33**	**0.60**	**0.55**	**1.82**	**1.83**	**0.037**	**0.053**	**0.72**	**0.037**	**0.14**
Error	±0.03	±0.04	±0.02	±0.05	±0.04	±0.006	±0.007	±0.2	±0.17	–

Table III. Summary of results of various experiments which obtained estimates of universal multifractal parameters for turbulent passive scalars in the atmosphere.

Reference	Field	Type	α	C_1	H
Finn *et al*. (2001)	SF_6	Time	1.65	0.11	0.40
Finn *et al*. (2001)	H_20	Time	1.60	0.07	–
Finn *et al*. (2001)	$^*T$	Time	1.69	0.09	0.44
Schmitt *et al*. (1996)	T	Time	1.45	0.07	0.38
Pelletier (1995)	T	Time	1.69	0.08	–
Pelletier (1995)	H_2O	Time	1.69	0.08	–
Wang (1995)	T	Time	1.69	0.10	0.41
Chigirinskaya *et al*. (1994)	T	Space (horizontal)	1.25	0.04	0.33
Schmitt *et al*. (1992)	T	Time	1.40	0.22	0.33
Average	Scalar	Time	1.64	0.085	0.41

* T = temperature

are not the averages of the values for the individual datasets, but are the values found from regression for the actual ensemble statistics.) H_z varies between 0.51 and 0.58 with an ensemble mean of 0.55 ± 0.02. Similar comparisons can be done for the other parameters. The ensemble means are arithmetic means with the exception of l_s, for which it is geometric. In part III we obtain similar estimates of l_s using meteorological models.

3.3. Comparison with other multifractal results on passive scalars

It is interesting to compare our parameter estimates with those of other passive scalars reported in the literature. Table III displays a number of other results. Caution should be used in this comparison, since, with only one exception, the literature values are for variations in time whereas we analyse (nearly) pure spatial data. Clearly it is not possible to make a strict and direct comparison between the results in this table and ours. In addition, the majority of the results were for temperature which is not obviously passive at all! Despite these limitations, there is fairly good quantitative agreement between the values obtained in the earlier studies and the values reported here. Since, as discussed in parts I, III there is a space–time anisotropy (if we ignore the effect of horizontal and vertical wind, it is characterized by $H_t = 2/3$ in the place of H_z), we should expect C_1, H to differ by factor H_t. However, as we discuss in part III, the time variation is often dominated by advection, in which case we expect C_1, H to have the horizontal values. From Table III, we find that while our α values are generally a little higher, those of C_1 are considerably higher. This may be a consequence of the fact that the lidar-measured concentration surrogate is actually nonlinearly related to the measured B; from Equation (11), if $\rho = B^\eta$, then we have $\alpha_\rho = \alpha_B$ but $C_{1\rho} = C_{1B}\eta^\alpha$; this is discussed in Lilley *et al*. (2004).

3.4. Analysis of the anisotropy

In multifractals there is a one-to-one correspondence between singularities (intensity levels) and statistical moments, hence by examining the stratification of both high- and low-order statistical moments, we are in fact determining whether both intense and weak structures are differentially stratified to the same degree (they have the same H_z). In Figure 9 we show H_z calculated directly from the ratios of structure function exponents, with the latter estimated both directly and from the Trace Moment technique discussed above. We see that the ratio

DOI: 10.1002/qj

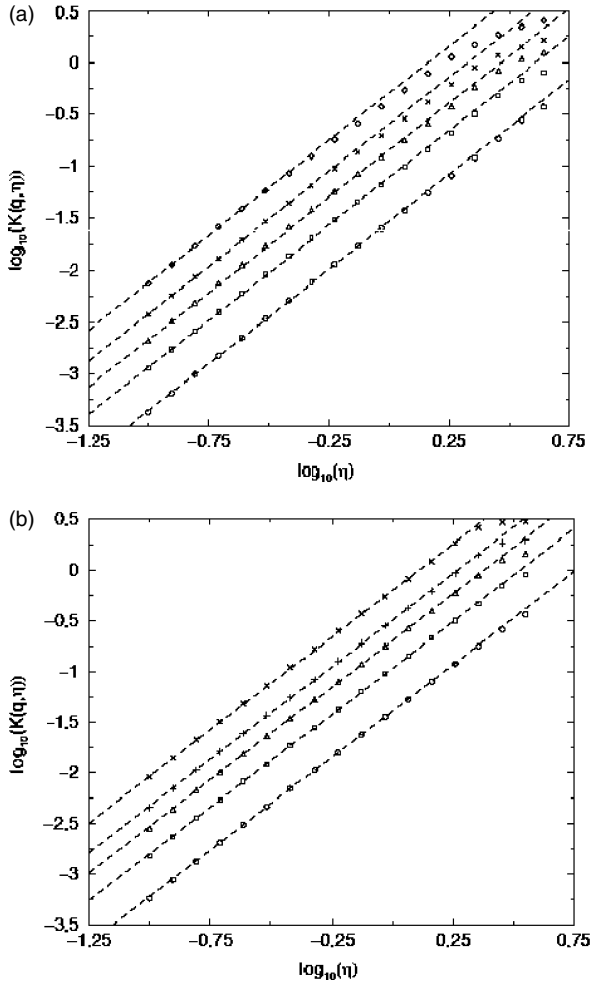

Figure 8. The (a) horizontal and (b) vertical $K(q,\eta)$ as a function of η. The regression lines have slopes $\alpha_h = 1.82$ in (a) and 1.83 in (b). The lines have different q values (1.5, 2.0, 2.5, 3.0, 4.0) from bottom to top in (a) and from top to bottom in (b).

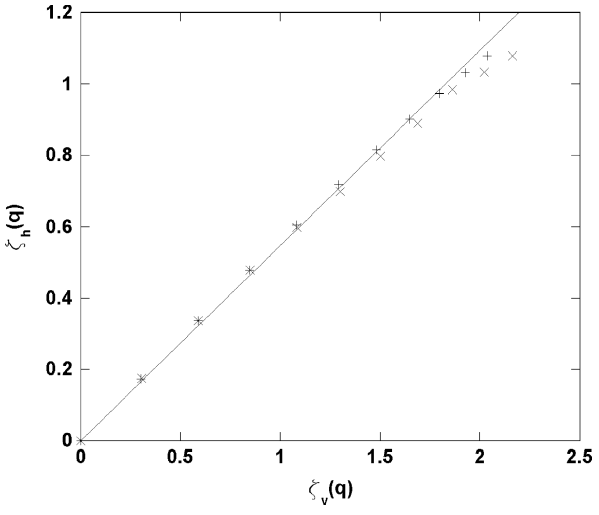

Figure 9. Scatterplots of $\xi_h(q)$ and $\xi_v(q)$ obtained for each cross-section using the trace moment method ($\times$) after adding qH, and directly from the structure functions ($+$). The reference line has slope $H_z = 5/9$.

of exponents is indeed nearly constant (all the points lie near the line of slope 5/9); we need to quantify the small deviations from this theoretical slope. In section

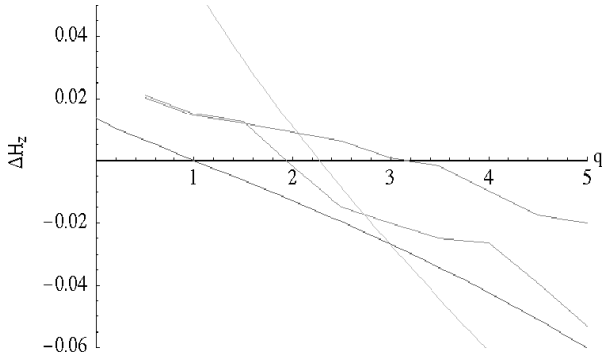

Figure 10. The intermittency correction to H_z as estimated from the horizontal and vertical $\xi(q)$ and $K(q)$ (top at right and second at right, respectively; from Figure 9). The top at left (smooth) curve is the estimate for the horizontal velocity based on multifractal parameters from a single pair of dropsonde estimates for the horizontal wind field (see part I appendix A), and the bottom at left (smooth) curve is the theoretical estimate based on the mean universal passive scalar parameters from Table II. This figure is available in colour online at www.interscience.wiley.com/qj

3.1 we quantified how H_z varied with q by introducing the deviation ΔH_z; this is shown in Figure 10. We see that the deviation is very small (of the order of -0.03 to $+0.02$, depending on q). One way to see whether these deviations are real or are due to experimental measurement error is to compare the two somewhat different analysis methods; in Figure 10 we see that their absolute difference is only noticeable for $q > 1.5$ and it stays <0.02 for q up to 5. We thus conclude that the basic trend is real.

Yet another way to quantify the accuracy of these very small exponent differences is to use the universal multifractal parametrization discussed in section 3.3. Recall that, in section 3.1, we showed how ΔH_z was related to $K_h(q)$, $K_v(q)$, noting that in the case of universal multifractals, ΔH_z could vanish for all q if $\alpha_h = \alpha_v$ and $C_{1h}/C_{1v} = 5/9$. Since in section 3.3 we empirically found that $\alpha_h \approx \alpha_v \approx 1.82$, the entire deviation ΔH_z depends on the deviation of C_{1h}/C_{1v} from the value 5/9. Putting this into Equation (10), we obtain:

$$\Delta H_z \approx \frac{1}{H_v} \frac{(H_{z,1} C_{1,v} - C_{1,h})(q^{\alpha-1} - 1)}{(\alpha - 1)} \qquad (15)$$

($\alpha = \alpha_h = \alpha_v$). Since empirically, we found $C_{1,h}/C_{1,v} \approx 0.7 \pm 0.2$, we expect a small non-zero ΔH_z. In Figure 10 we see that, using the mean parameters, we indeed obtain a close but non-identical curve; one reason for the non-coincidence is that the universal multifractal parametrization assumes $K(1) = 0$ so that $\Delta H_z(1) = 0$, whereas the direct estimates find it to be a little larger.

4. Conclusions

One of the most basic aspects of atmospheric structure is its spatial stratification. In part I we discussed various models and proposed a new one – a turbulence/wave generalization of the classical 23/9-D model in which

DOI: 10.1002/qj

the stratification is differential, i.e. the typical 'flatness' or anistropy of structures increases with scale in a scaling way, i.e. without characteristic length-scale. In this paper (part II), we considered the experimental evidence, first reviewing the data on horizontal and vertical statistics; we argued that they were compatible with the value $D_s = 23/9$ rather than 2, 3 or 7/3 (the competing 2-D, 3-D and linear gravity wave theories respectively); in part III (Radkevich *et al*., 2008) we investigate the stratification of the full space–time. However, the classical evidence on stratification is indirect; the only direct way to investigate the stratification is through vertical cross-sections. With the advent of high-powered lidars with logarithmic amplifiers, this is now possible. Here we studied stratified structures spanning over three orders of magnitude in both horizontal and vertical scales. Using such state-of-the-art lidar data, Lilley *et al*. (2004) made the first direct measurements of the elliptical dimension D_s characterizing the stratification finding that it is $D_s = 2.55 \pm 0.02$, which is very close to the theoretically predicted value $23/9 = 2.555\ldots$, but quite far from the standard values 2 (completely flat) or 3 (completely isotropic). In this paper, we extend the Lilley *et al*. (2004) study by examining the stratification of both high- and low-order statistical moments, we showed that both intense and weak structures were apparently differentially stratified to the same degree (same H_z).

The 'unified scaling' or '23/9-D' theory which predicts this result is based on the primacy of buoyancy forces in determining the vertical structure while allowing energy fluxes to determine the horizontal structure. It predicts the observed wide-range scaling in cloud radiances, and – as our review shows – it is compatible with the available observations of both the horizontal and vertical wind and temperature spectra. In contrast, the standard model does not directly consider the buoyancy at all and it involves two isotropic regimes – at small scales it is 3-D energy driven, while at large scales it is 2-D and both enstrophy and energy driven. The model also explains the difficulty in making aircraft measurements of horizontal structure: 23/9-D turbulence can lead to fractal aircraft trajectories (the result of long-range correlations between the trajectory and the atmospheric variables), hence to long-range biases so that the spectra may be incorrectly interpreted. In addition, a very small average vertical gradient leads to a transition from $k^{-5/3}$ to $k^{-11/5}$; we quantitively showed this on the two major campaigns to date: GASP and MOZAIC. Finally, the 23/9-D model naturally explains how the horizontal structures in the atmosphere can display wide-range scaling, right through the mesoscale.

The 23/9-D turbulent model is physically satisfying since it finally allows buoyancy to play the role of fundamental driver of the dynamics. With the allowance for a wave-like fractional integration, it can be compatible with gravity wave phenomenology. While to numerical weather forecasters the dimension of stratification may seem academic, until now virtually all turbulent theories have been very nonlinear (energy or enstrophy flux driven), while the mainstream interpretations of the data have been in terms of (quasi-) linear waves. Our model and empirical findings thus promise a more theoretically satisfying overall (large- to small-scale) picture of atmospheric dynamics. The full implications of the model may take many years to discern. For the classical numerical models, the challenge will be either to show that the existing stratification assumptions (e.g. the hydrostatic, anelastic or Boussinesq approximations) lead to realistic anisotropic scaling, or to replace them with approximations which are. Conversely, in part I we showed that it was not so hard to use such a realistic stratification in stochastic multifractal models; for these, the challenge is to go beyond a scalar framework to incorporate other atmospheric fields using the notion of 'state vectors' and Lie cascades (Schertzer and Lovejoy, 1995).

References

Adelfang SI. 1971. On the relation between wind shears over various intervals. *J. Appl. Meteorol.* **10**: 156–159.

Allen SJ, Vincent RA. 1995. Gravity wave activity in the lower atmosphere: Seasonal and latitudinal variations. *J. Geophys. Res.* **100**: 1327–1350.

Beatty TJ, Hostletler CA, Gardner CS. 1992. Lidar observations of gravity waves and their spectra near the mesopause and stratopause at Arecibo. *J. Atmos. Sci.* **49**: 477–496.

Bolgiano R. 1959. Turbulent spectra in a stably stratified atmosphere. *J. Geophys. Res.* **64**: 2226–2229.

Brown PS, Robinson GD. 1979. The variance spectrum of tropospheric winds over Eastern Europe. *J. Atmos. Sci.* **36**: 270–286.

Chigirinskaya Y, Schertzer D, Lovejoy S, Lazarev A, Ordanovich A. 1994. Unified multifractal atmospheric dynamics tested in the tropics. Part 1: Horizontal scaling and self organized criticality. *Nonlinear Processes in Geophysics* **1**: 105–114.

Cho JYN, Lindborg E. 2001. Horizontal velocity structure functions in the upper troposphere and lower stratosphere. I. Observations. *J. Geophys. Res.* **106**(D10): 10223–10232.

Corrsin S. 1951. On the spectrum of isotropic temperature fluctuations in an isotropic turbulence. *J. Appl. Phys.* **22**: 469–473.

Cot C. 2001. Equatorial mesoscale wind and temperature flluctuations in the lower atmosphere. *J. Geophys. Res.* **106**: 1523–1532.

Endlich RM, Singleton RC, Kaufman JW. 1969. Spectral analyses of detailed vertical wind profiles. *J. Atmos. Sci.* **26**: 1030–1041.

Finn D, Lamb B, Leclerc MY, Lovejoy S, Pecknold S, Schertzer D. 2001. Multifractal analysis of plume concentration fluctuations in surface layer flows. *J. Appl. Meteorol.* **40**: 229–245.

Fritts DC, Chou H-G. 1987. An investigation of the vertical wavenumber and frequency spectra of gravity wave motions in the lower stratosphere. *J. Atmos. Sci.* **44**: 3610–3624.

Fritts DC, Tsuda T, Sato T, Fukao S, Kato S. 1988. Observational evidence of a saturated gravity wave spectrum in the troposphere and lower stratosphere. *J. Atmos. Sci.* **45**: 1741–1759.

Gage KS, Nastrom GD. 1986. Theoretical interpretation of atmospheric wavenumber spectra of wind and temperature observed by commercial aircraft during GASP. *J. Atmos. Sci.* **43**: 729–740.

Gao X, Meriwether JW, Wickwar VB, Wilkerson TD, Collins S. 1998. Rayleigh lidar measurements of the temporal frequency and vertical wavenumber spectra in the mesosphere over the Rocky Mountain region. *J. Geophys. Res.* **103**(D6): 6405–6416.

Gardner CS. 1994. Diffusive filtering theory of gravity wave spectra in the atmosphere. *J. Geophys. Res.* **99**: 20601–20622.

Gardner CS, Tao X, Papen GC. 1995. Simultaneous lidar observations of vertical wind, temperature and density profiles in the upper atmsophere: Evidence of nonseparability of atmospheric perturbation spectra. *Geophys. Res. Lett.* **22**(20): 2877–2880.

Garrett C, Munk W. 1972. Space-time scales of internal waves. *Geophys. Fluid Dyn.* **2**: 225–264.

Goldman JL. 1968. 'The power spectrum in the atmosphere below macroscale'. Institute of Desert Research, University of St. Thomas: Houston, Texas.

Hwang HJ. 1970. Power density spectrum of surface wind speed on Palmyra island. *Mon. Weather Rev.* **98**: 70–74.

DOI: 10.1002/qj

Lavallée D, Lovejoy S, Schertzer D, Ladoy P. 1993. Nonlinear variability and landscape topography: analysis and simulation. Pp. 171–205 in *Fractals in Geography.* De Cola L, Lam N. (eds). Prentice-Hall: Englewood, New Jersey.

Lazarev A, Schertzer D, Lovejoy S, Chigirinskaya Y. 1994. Unified multifractal atmospheric dynamics tested in the tropics. Part II: Vertical scaling and generalized scale invariance. *Nonlinear Processes in Geophysics* **1**: 115–123.

Lilley M. 2003. 'Lidar measurements of passive scalars and the 23/9-dimensional model of atmospheric dynamics'. MSc thesis. p. 145 in *Physics,* McGill University: Montreal.

Lilley M, Lovejoy S, Strawbridge K, Schertzer D. 2004. 23/9 dimensional anisotropic scaling of passive admixtures using lidar aerosol data. *Phys. Rev. E* DOI 10.1103/70, 036307-1-7.

Lindborg E, Cho JYN. 2001. Horizontal velocity structure functions in the upper troposphere and lower stratosphere. II. Theoretical considerations. *J. Geophys. Res.* **106**(D10): 10233–10242.

Lovejoy S. 1982. Area perimeter relations for rain and cloud areas. *Science* **187**: 1035–1037.

Lovejoy S, Schertzer D. 2006. Multifractals, cloud radiances and rain. *J. Hydrol.* DOI: 10.1016/j.hydrol.2005.02.042.

Lovejoy S, Schertzer D, Tsonis AA. 1987. Functional box-counting and multiple dimensions in rain. *Science* **235**: 1036–1038.

Lovejoy S, Schertzer D, Silas P, Tessier Y, Lavallée D. 1993. The unified scaling model of atmospheric dynamics and systematic analysis in cloud radiances. *Annales Geophysicae* **11**: 119–127.

Lovejoy S, Schertzer D, Stanway JD. 2001. Direct evidence of planetary scale atmospheric cascade dynamics. *Phys. Rev. Lett.* **86**: 5200–5203.

Lovejoy S, Schertzer D, Tuck AF. 2004. Fractal aircraft trajectories and nonclassical turbulent exponents. *Physical Review E* DOI 10.1103/70, 036306-1-5.

Lovejoy S, Tuck AF, Hovde SJ, Schertzer D. 2007. Is isotropic turbulence relevant in the atmosphere? *Geophys. Res. Lett.* **34**: L14802, DOI: 10.1029/2007GL029359.

Lovejoy S, Schertzer D, Allaire V. 2008a. The remarkable wide range spatial scaling of TRMM precipitation. *J. Atmos. Res.* in press.

Lovejoy S, Schertzer D, Allaire V, Bourgeois T, King S, Pinel J, Stolle J. 2008b. The remarkable wide range spatial scaling of atmospheric radiances. *Phys. Rev. Lett.* submitted.

Lovejoy S, Schertzer D, Lilley M, Strawbridge KB, Radkevich A. 2008c. Scaling turbulent atmospheric stratification. I: Turbulence and waves. *Q. J. R. Meteorol. Soc.* **134**: ???–???.

Obukhov A. 1949. Structure of the temperature field in a turbulent flow. *Izv. Akad. Nauk. SSSR. Ser. Geogr. I Geofiz* **13**: 55–69.

Obukhov A. 1959. Effect of Archimedean forces on the structure of the temperature field in a turbulent flow. *Dokl. Akad. Nauk SSSR* **125**: 1246.

Pelletier J. 1995. 'Multifractal characterization of aircraft-based measurements of turbulence and passive scalar fields within the surface boundary layer'. In *Atmospheric and Oceanic Sciences.* McGill University: Montreal.

Pinus NZ. 1968. The energy of atmospheric macro-turbulence. *Izvestiya, Atmospheric and Oceanic Physics* **4**: 461.

Radkevich A, Lovejoy S, Strawbridge KB, Schertzer D, Lilley M. 2008. Scaling turbulent atmospheric stratification. III: Space-time stratification of passive scalars from lidar data. *Q. J. R. Meteorol. Soc.* **134**: ???–???.

Schertzer D, Lovejoy S. 1985. The dimension and intermittency of atmospheric dynamics. Pp. 7–33 in *Turbulent Shear Flow 4* Launder B (ed). Springer-Verlag.

Schertzer D, Lovejoy S. 1987. Physical modeling and analysis of rain and clouds by anisotropic scaling of multiplicative processes. *J. Geophys. Res.* **92**: 9693–9714.

Schertzer D, Lovejoy S. 1995. From scalar cascades to Lie cascades: Joint multifractal analysis of rain and cloud processes. Pp. 153–173 in *Space/time variability and interdependance for various hydrological processes.* Feddes RA (ed). Cambridge University Press: New York.

Schertzer D, Lovejoy S. 1997. Universal multifractals do exist! *J. Appl. Meteorol.* **36**: 1296–1303.

Schertzer D, Lovejoy S, Lavallée D. 1993. Generic multifractal phase transitions and self-organized criticality. Pp. 216–227 in *Cellular Automata: prospects in astronomy and astrophysics.* Perdang JM, Lejeune A (eds). World Scientific.

Smith SA, Fritts DC, VanZandt TE. 1987. Evidence for a saturated spectrum of atmospheric gravity waves. *J. Atmos. Sci.* **44**: 1404–1410.

Schmitt F, Lovejoy S, Schertzer D, Lavallée D, Hooge C. 1992. First estimates of multifractal indices for velocity and temperature fields. *Comptes Rendus de l'Académie des Sciences de Paris, serie II* **314**: 749–754.

Schmitt F, Schertzer D, Lovejoy S, Brunet G. 1996. Universal multifractal structure of atmospheric temperature and velocity fields. *Europhysics Lett.* **34**: 195–200.

Taylor GI. 1938. The spectrum of turbulence. *Proc. R. Soc. London A* **164**: 476–490.

Tsuda T, Inoue T, Kato S, Fukao S, Fritts DC, VanZandt TE. 1989. MST radar observations of a saturated gravity wave spectrum. *J. Atmos. Sci.* **46**: 2440–2447.

Van der Hoven I. 1957. Power spectrum of horizontal wind speed in the frequency range from.0007 to 900 cycles per hour. *J. Meteorol.* **14**: 160–164.

VanZandt TE. 1982. A universal spectrum of buoyancy waves in the atmosphere. *Geophys. Res. Lett.* **9**: 575–578.

Vinnichenko NK. 1969. The kinetic energy spectrum in the free atmosphere for 1 second to 5 years. *Tellus* **22**: 158–166.

Wang Y. 1995. 'Measurements and multifractal analysis of turbulent temperature and velocity near the ground'. In *Atmospheric and Oceanic Sciences*. McGill University: Montreal.